Contents lists available at ScienceDirect

Mechatronics

journal homepage: www.elsevier.com/locate/mechatronics

Control of on-demand nanoliter drop volume and jetting velocity in piezoelectric inkjet printing

Jie Wang, George T.-C. Chiu *

School of Mechanical Engineering, Purdue University, 585 Purdue Mall, West Lafayette, 47907, IN, USA

ARTICLE INFO

Keywords:
Inkjet printing
Additive manufacturing
Stochastic systems
Kalman filter
Process control

ABSTRACT

Consistent dosages placed with high accuracy onto the substrate are critical for drop-on-demand (DoD) inkjet printing to be adopted in additive manufacturing and device characterization. Practically, the consistency of drop volume and drop jetting velocity is subject to process uncertainties, such as fluctuations of applied pressure and variations in printheads, for which open-loop approaches are unable to compensate. In this work, a stochastic process model of the relation between two control parameters of a firing waveform and two output features, drop volume and drop jetting velocity, is developed from standard printhead calibration data. An image-based control strategy based on a projection-based one-step-ahead Kalman estimator for model parameters estimation is proposed to regulate the drop volume and the drop jetting velocity. The effectiveness of the proposed control strategy is experimentally validated for three inks with broad properties. By including input boundary layers, an order of magnitude improvement in reducing drop volume and jetting velocity variations is also experimentally demonstrated.

1. Introduction

Drop-on-demand (DoD) inkjet printing, which is characterized by small drops controlled in an on-demand fashion, has been extensively seen in many applications, such as drug delivery [1,2] and functionalization of electrochemical and microfluidics devices [3–6]. These applications require the inkjet printing system to deliver and pattern functional materials with precise volume on the substrate at a constant jetting velocity.

Studies of drop dynamics in DoD inkjet printing have been reported for decades [7–9], aiming at understanding fluid response to the actuating signal. The actuating signal given in commercial printheads is typically a parameterized waveform, only a few control parameters of which are accessible and can be adjusted by users. For applications using commercial printheads, tuning the control parameters through trial-and-error and designing new parameterized waveforms to achieve desired drop behaviors are more straightforward and practical [10,11]. Model-based and experiment-driven waveform optimization approaches were proposed by Khalate et al. [12,13] and Ezzeldin et al. [14] to improve drop velocity consistency at a broad range of jetting frequencies. Uncertainties in DoD inkjet printing, such as tolerance of the nozzle size and fluctuations of supply pressure and environmental conditions, result in variations in drop characteristics in practice. Tomaszewski et al. [15] and Kiefer et al. [16] reported that print results differ from nozzles and times. Hass et al. [17] and Tröndle et al. [18] obtained high relative standard deviations (RSDs) of drop volume when they fabricated nuclear targets and bio-structures, respectively. An empirical example is shown in Fig. 1, where fluctuations of drop volume and drop jetting velocity were observed by authors using the same nozzle and the same firing waveform at different times for DI water, color ink and glycerol–water mixture, respectively. Wide spreads of the drop volume and drop jetting velocity can interpret the varying printed results.

Since open-loop methods cannot address process uncertainty efficiently, feedback approaches were proposed. Barton et al. [19] developed a control and sensing strategy in electrohydrodynamic jet printing to compensate for uncertainty in jetting operating conditions. In [20], a neural network was introduced to associate drop behaviors with drive voltages, and then a PID controller was used in [20] to control the drop behavior via the voltage.

Wang et al. [21] modeled the relationship between one control parameter of a firing waveform and drop volume in a static function and proposed an image-based PI controller to regulate the drop volume. By incorporating the control to drop jetting velocity, Wang et al. [22] further derived a two-input two-output stochastic model from standard printhead calibration data and constructed a control strategy to regulate the drop volume and the drop jetting velocity. The associated analyses of stability and parameter convergence were

* Corresponding author.
E-mail addresses: wang2474@purdue.edu (J. Wang), gchiu@purdue.edu (G.T.-C. Chiu).

https://doi.org/10.1016/j.mechatronics.2023.103031
Received 31 January 2023; Received in revised form 30 May 2023; Accepted 10 July 2023

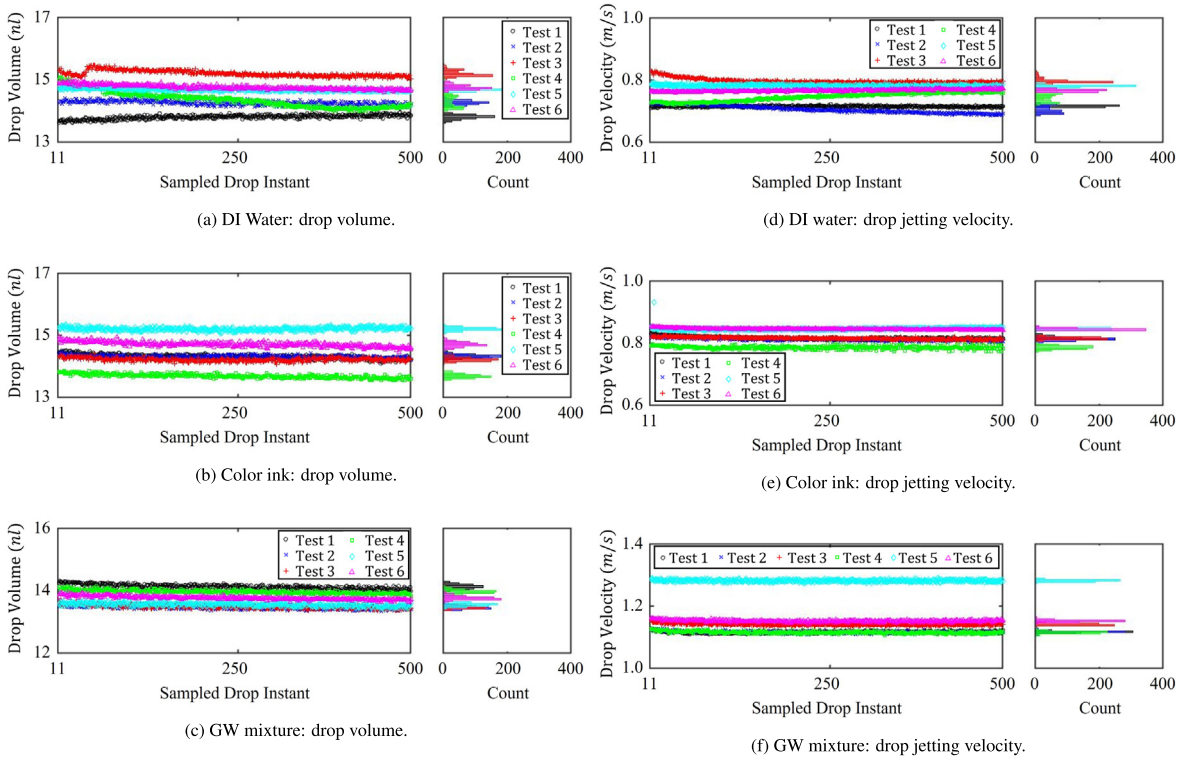

(a) DI Water: drop volume.

(b) Color ink: drop volume.

(c) GW mixture: drop volume.

(d) DI water: drop jetting velocity.

(e) Color ink: drop jetting velocity.

(f) GW mixture: drop jetting velocity.

Fig. 1. Drop volumes and jetting velocities of DI water, color ink, and glycerol–water mixture using the same nozzle with the same firing waveform, respectively, at different times.

detailed in [23]. This paper expands the experimental-base modeling outlined in [22,23] by providing detailed analysis and experimental validation of the methods used to accomplish real-time computation of drop volume and drop jetting velocity for real-time control. Experimental results and input–output analysis in [23] suggest room to further improve the controller performance in reducing output variations. In this work, an improvement to the control algorithm developed in [22, 23] is presented by introducing boundary layers in the control input to reduce output variations. Experimental validation using three different inks/materials confirms the effectiveness of the proposed modification with properly selected boundary layers (described in Section 5), where up to 19% further reduction in output variation can be achieved.

The remainder of this paper is structured as follows. The printing system is introduced in Section 2, followed by the system model development. Section 4 shows the control strategy. Experimental validation of the control algorithm is given in Section 5 followed by the conclusion.

2. Printing system

A commercial piezo-driven nanoliter inkjet printhead is used in this study (BioFluidix PipeJet, Freiburg, Germany). The printhead nozzle is a disposable elastic polymer pipe clamped between two guide plates, see Fig. 2, one end of which is connected to a syringe barrel as an ink reservoir, where back pressure can be applied. Ink is jetted out at the other open end controlled by the displacement of a piezostack-driven piston [24]. The piston displacement can be described as a preset trapezoidal waveform [25], see Fig. 3, which is parameterized by four parameters: stroke velocity u_1, the rate of piston movement; piston stroke u_2, the distance the piston will move; instroke velocity u_3, which is associated with the printing frequency; and stroke holding time t_H. Among them, u_1 and u_2 are the control inputs/parameters which can be adjusted by users to regulate the drop volume and the jetting velocity. The stroke velocity u_1 primarily changes the drop jetting velocity, and the μm- scale stroke u_2 influences the drop volume more, see Fig. 6.

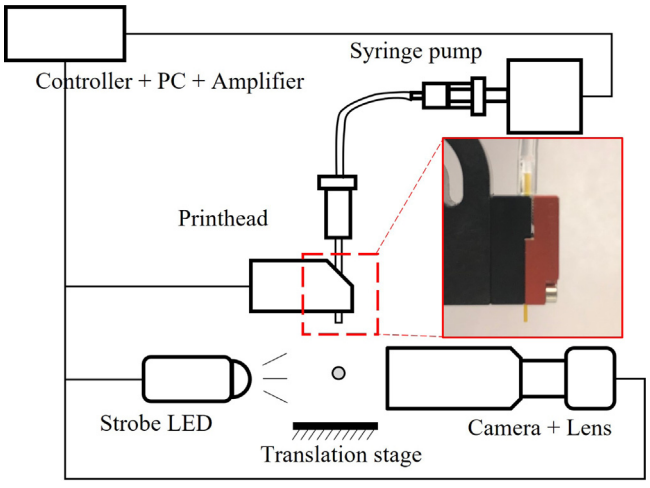

Fig. 2. Schematic of the printing system.

The printing system also comprises a translation stage to move the substrate for pattern generation, a monochrome camera (Flea3 FL3-U3-13Y3M) with a 1X telecentric lens, a NI myRIO embedded device (National Instruments), a strobe LED, a homemade syringe pump for pressure regulation in the reservoir, and a PC. The printer, camera, and strobe LED are synchronized by a trigger signal generated by processing the stage encoder output through an FPGA. Strobe-illuminated drops at different distances away from the nozzle can be observed by changing the trigger delay to the camera. The optical system used in this study has a resolution of 1.3 megapixels with a pixel size of 4.73 μm which is calibrated by a 0.25 mm Thorlabs R2L2S3P2 grid distortion target.

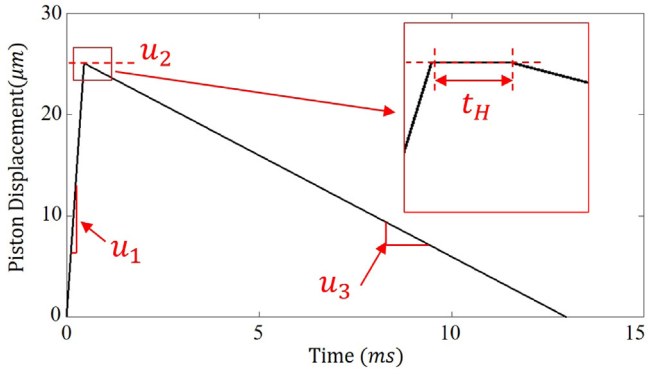

Fig. 3. A parameterized waveform to the printhead, where stroke velocity u_1 = 55 μm/ms, stroke u_2 = 25 μm, instroke velocity u_3 = 2 μm/ms, and stroke holding time t_H = 20 μs.

3. System model development

Although first-principle models detail drop formation, their complexity and limited accessible control parameters provided in commercial printheads make these models difficult for controller design [26]. Instead, using the experimental data collected in waveform tuning practice for matching the ink and the printhead, a data-driven control-oriented model can be derived by mapping the control parameters onto the measured drop characteristics.

3.1. Drop volume and jetting velocity estimations

Stroboscopic technique has been widely used to observe drop formation in DoD inkjet printing [10,25,27], where a strobe LED is synchronized with the drop firing trigger signal to illuminate an in-flight drop and ensure an appropriately-exposed drop image. Fig. 4(a) shows an example of an in-flight drop that is stroboscopically illuminated and acquired at a strobe trigger delayed by 1.8 ms from the drop firing trigger signal. To further separate drop profile from its background, image processing and analysis steps are needed.

3.1.1. Drop volume estimation

Fig. 4(a) shows the image processing steps for estimating drop volume. A region of interest (ROI) containing the drop and the nozzle tip is first identified and cropped from the acquired image. Otsu's method is then used to identify the appropriate threshold to convert the grayscale ROI image into a binary image [28]. Additional image filtering and extraction are applied to isolate the drop and identify its axis of symmetry. The drop profile is rotated by aligning its axis of symmetry to the vertical axis of the image. Assuming that the in-flight drop is incompressible and rotationally symmetric with respect to the axis of symmetry, a rotationally symmetric model is used to estimate the drop volume [21,27,29]. Fig. 4(b) shows that the drop profile is sliced into one-pixel-height disks along the axis of symmetry. The distance between the two outermost edge pixels of a disk is defined as the diameter of the disk. The volume of the ith disk, V_i, is computed by

$$V_i = \frac{\pi h d_i^2}{4}, \tag{1}$$

where d_i is the diameter in pixel of the ith disk and h is the pixel height, which is one in this work. Assuming that the drop is H pixels high, the estimated drop volume is

$$V = \sum_{i=1}^{H} V_i. \tag{2}$$

Uneven back illuminance across the field of view of the imaging system introduces uncertainty in edge identification when the drop is imaged at different distances away from the nozzle. Assuming the diameter d_i of the ith disk is offset by Δd_i pixels, where $\Delta d_i \le d_i$, the volume uncertainty can be calculated as

$$\Delta V = \frac{\pi h}{4} \sum_{i=1}^{H} \left(d_i^2 - (d_i - \Delta d_i)^2 \right). \tag{3}$$

The uncertainty in edge identification not only accounts for the accuracy of volume estimation but also implies the potential variation in identifying the geometric centroid of the drop profile.

A gravimetric method was utilized to verify the volume estimation algorithm by jetting 500, 600 and 800 drops of DI water at a constant pair of stroke velocity 70 μm/ms and stroke 25 μm, see Table 1. In each test, drops fired at 1 Hz were collected with a pre-weighed 1.5 ml microcentrifuge tube at room temperature. Once the collection was completed, the tube lid was immediately closed to prevent further liquid evaporation. The filled tube was weighed five times using an analytical balance (Radwag AS 82/220.X2). The corresponding volume per drop was calculated with the density of DI water listed in Table 2.

While collecting the drops with the tube, each drop was stroboscopically illuminated in flight and imaged for volume estimation. To account for the uncertainty associated with uneven back illuminance, an additional increment of 10 μs strobe trigger delay was added to each consecutive drop to ensure drop images were acquired along the field of view. Eq. (2) was used to estimate the volume of each drop. Table 1 shows drop volume based on image estimation, Eq. (2), and gravimetric measurement, respectively. As can be seen, the drop volume calculated from Eq. (2) is an acceptable real-time estimation of drop volume, where its mean value is within 1.5% (less than 0.2 nl) from that of gravimetric measurement.

3.1.2. Drop jetting velocity estimation

By illuminating in-flight drops at different strobe trigger delays, their locations relative to the nozzle tip can be obtained, as illustrated in Fig. 5. The difference between locations, Δz in Fig. 5, can be obtained from consecutive drop images. Since the time difference Δt between trigger delays for the consecutive images is also known, the drop jetting velocity can be estimated by

$$y^{vel} = \frac{\Delta z}{\Delta t}, \tag{4}$$

where Δz is the relative distance between two drop centroids identified from two consecutive drop images, and Δt is the difference between strobe LED delays to the two consecutive images.

3.2. System modeling

In DoD inkjet printing, a commercial printhead and inks/materials are matched through a calibration process. Since only a few control parameters are typically made available to the users by the printhead manufacturers, the calibration process involves varying the accessible control parameters through a grid pattern to identify printable regions of control parameters for the specified drop characteristics, such as volume and jetting velocity. This practice also includes acquiring multiple stroboscopic drop images at each set of control parameters for drop characterization.

Using the methods described in the previous section, drop volumes and jetting velocities associated with different sets of control parameters can be estimated from images and data collected from the calibration process. By mapping drop characteristics to their associated control parameters, input–output relationships between the control parameters and the drop characteristics can be identified.

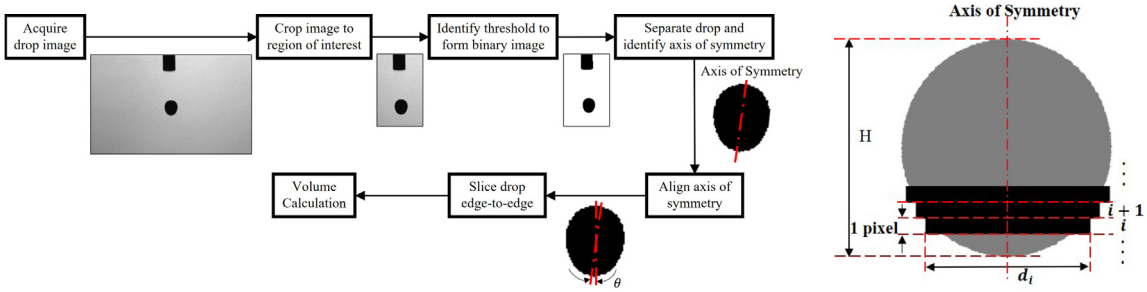

(a) Image processing steps. (b) Model of drop volume estimation.

Fig. 4. Image processing outline for drop volume estimation.

Table 1
Comparison between image estimation and gravimetric measurement of drop volumes at stroke velocity $u_1 = 70$ μm/ms and stroke $u_2 = 25$ μm.

Test	Total jetted drops	Image estimation (nl)	Gravimetric measurement (nl)	Discrepancy of mean (%)
1	500	13.08 ± 0.326	12.90 ± 0.065	1.40
2	500	13.61 ± 0.356	13.59 ± 0.090	0.15
3	600	13.47 ± 0.290	13.42 ± 0.064	0.37
4	600	13.48 ± 0.287	13.34 ± 0.054	1.05
5	800	13.58 ± 0.314	13.48 ± 0.053	0.74
6	800	13.50 ± 0.262	13.38 ± 0.034	0.90

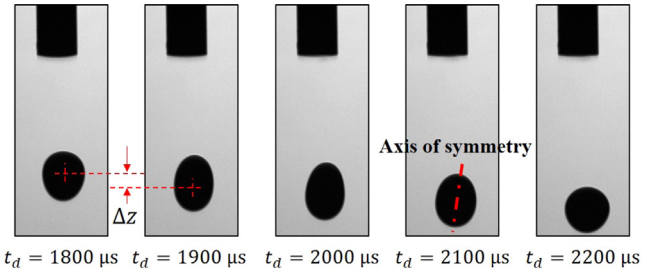

Fig. 5. A sequence of stroboscopic drop images captured at different strobe delays t_d for constant control parameters, stroke velocity u_1 and stroke u_2.

Table 2
List of ink physical properties and experimental parameters.

Name	DI water	Color ink	GW mixture
Density (g/cm^3)	1.002	0.993	1.158
Viscosity (mPa s)	1.07	2.21	9.53
Surface Tension (mN/m)	73.24	28.72	67.87
Back Pressure (Pa)	0	−500	−100
Stroke Velocity u_1 Range (μm/ms)	60–75	50–80	70–100
Stroke Velocity u_1 Increment (μm/ms)	1.25	5	2.5
Stroke u_2 Range (μm)	20–35	20 – 35	25–35
Stroke u_2 Increment (μm)	1.25	1.25	1.25

3.2.1. Printhead-ink calibration experiments

Three inks were tested with the PipeJet printhead in this study: deionized (DI) water, pigmented color ink (INKUTEN Premium Pigmented Sublimation ink), and glycerol–water (GW) mixture of 60 wt% glycerol and 40 wt% DI water. They represent different densities, viscosities and surface tensions that are commonly used in DoD inkjet printing. Table 2 gives their densities (calculated by a sample mass divided by the associated given volume), viscosities (measured by a viscometer, microVISC, RheoSense, INC), and surface tensions (measured by a tensiometer, Krüss DSA 100, Germany), which were measured at room temperature 22.7°C. To form a stable meniscus, back pressure for each ink was measured by an inline differential pressure sensor and maintained at the setpoint with less than ±5 Pa variations using a syringe pump driven by a PID-controlled voice coil motor.

In this study, printable regions for control parameters u_1 and u_2 were selected, where acceptable jetting behaviors were observed, i.e., no satellite drops and no unstable tails, see Table 2. At each pair of control parameters (u_1, u_2), at least two hundred drops were jetted and imaged at different strobe delays in increments of 10 μs from the instant when the drop was pinched off from the nozzle to the instant when the drop fell out of the field of view. With drop volumes and jetting velocities estimated from these images, input–output maps of drop characteristics for the inks under test were generated with respect to control input pairs (u_1, u_2), see Fig. 6.

3.2.2. Drop volume data

Figs. 6(a), (c) and (e) show the mean of drop volumes estimated by Eq. (2) with one standard deviation at different pairs of stroke velocity u_1 and stroke u_2 of DI water, color ink, and GW mixture, respectively. The data suggest that the drop volume is linearly dependent on stroke velocity u_1 and stroke u_2, i.e., the drop volume y^{vol} can be presented by a linear equation,

$$y^{vol} = g_{11} \cdot u_1 + g_{12} \cdot u_2 + f_1, \tag{5}$$

where g_{11} and g_{12} are the coefficients of stroke velocity u_1 and stroke u_2, respectively, and f_1 is the bias. The linear models were validated by 10-fold cross validation and drawn as gray hyperplanes in Figs. 6(a), (c) and (e) with the approximated coefficients from the least squares regression. The hyperplanes verify that stroke u_2 impacts drop volume more than stroke velocity u_1. Drop volumes of the DI water have larger fluctuations in comparison with drop volumes of the other two inks. Large process uncertainties mainly account for these fluctuations.

3.2.3. Drop jetting velocity data

Figs. 6(b), (d) and (f) show the average of drop jetting velocities calculated by Eq. (4) with one standard deviation at different pairs of stroke velocity u_1 and stroke u_2 of DI water, color ink, and GW mixture, respectively. Similar to drop volume, the data in Figs. 6(b), (d) and (f) suggest that a linear hyperplane can be used to relate drop jetting velocity to stroke velocity u_1 and stroke u_2,

$$y^{vel} = g_{21} \cdot u_1 + g_{22} \cdot u_2 + f_2, \tag{6}$$

where g_{21} and g_{22} are the coefficients of stroke velocity u_1 and stroke u_2, respectively, and f_2 is the bias. The linear hyperplanes were also validated by 10-fold cross validation and drawn in gray as shown in Figs. 6(b), (d) and (f) using the approximated coefficients from the least squares regression. The hyperplanes confirm that stroke velocity

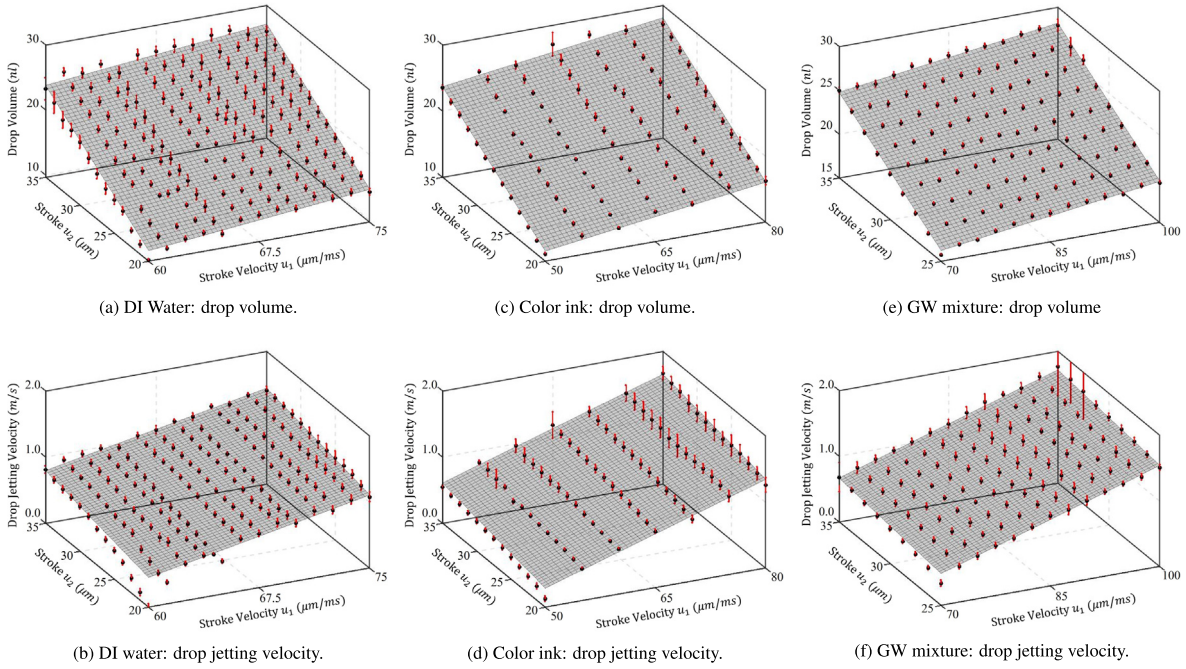

(a) DI Water: drop volume. (c) Color ink: drop volume. (e) GW mixture: drop volume

(b) DI water: drop jetting velocity. (d) Color ink: drop jetting velocity. (f) GW mixture: drop jetting velocity.

Fig. 6. In-flight drop volumes (nl) and drop jetting velocities (m/s) of DI water, color ink, and GW mixture with respect to pairs of control parameters/inputs (u_1, u_2): Black dots are mean values, red bars represent one standard deviations, and gray planes are first-order fitting hyperplanes.

u_1 has more influence on drop jetting velocity than stroke u_2. Large fluctuations of drop jetting velocity are found in the experiments with high stroke velocity u_1. It is mainly due to the large variation in the calculated centroid velocity during the notable recoil of the drop jetted with high forward momentum.

3.2.4. Data-driven modeling

A two-input two-output static model can be formed by combining Eqs. (5) and (6),

$$Y = \begin{bmatrix} y^{vol} \\ y^{vel} \end{bmatrix} = F + G\bar{U} = \begin{bmatrix} f_1 \\ f_2 \end{bmatrix} + \begin{bmatrix} g_{11} & g_{12} \\ g_{21} & g_{22} \end{bmatrix} \begin{bmatrix} u_1 \\ u_2 \end{bmatrix}$$
$$= U\Theta = \begin{bmatrix} 1 & 0 & u_1 & u_2 & 0 & 0 \\ 0 & 1 & 0 & 0 & u_1 & u_2 \end{bmatrix} \begin{bmatrix} f_1 \\ f_2 \\ g_{11} \\ g_{12} \\ g_{21} \\ g_{22} \end{bmatrix}, \tag{7}$$

where Y is the output vector, F is the system bias vector, G is the system gain matrix, $\bar{U}$ is the system input vector, U is the input matrix, and Θ is the model parameter vector which consists of the bias F and the system gain G. With the experimental data presented in Fig. 6, the nominal model parameters F_o and G_o or equivalently Θ_o approximated from linear least squares regression are

for DI water,

$$G_o = \begin{bmatrix} 0.23_{(\pm 0.002)} & 0.83_{(\pm 0.002)} \\ 0.049_{(\pm 0.003)} & 0.025_{(\pm 0.003)} \end{bmatrix}, \quad F_o = \begin{bmatrix} -18.97_{(\pm 0.017)} \\ -3.08_{(\pm 0.18)} \end{bmatrix},$$

for color ink,

$$G_o = \begin{bmatrix} 0.15_{(\pm 0.001)} & 0.81_{(\pm 0.002)} \\ 0.035_{(\pm 0.001)} & 0.021_{(\pm 0.002)} \end{bmatrix}, \quad F_o = \begin{bmatrix} -12.06_{(\pm 0.065)} \\ -1.87_{(\pm 0.067)} \end{bmatrix}, \tag{8}$$

and for glycerol–water mixture,

$$G_o = \begin{bmatrix} 0.11_{(\pm 0.001)} & 0.85_{(\pm 0.002)} \\ 0.035_{(\pm 0.001)} & 0.020_{(\pm 0.001)} \end{bmatrix}, \quad F_o = \begin{bmatrix} -13.05_{(\pm 0.060)} \\ -2.51_{(\pm 0.060)} \end{bmatrix},$$

where subscripts are the 95% confidence interval errors.

To remove the drifting trend and various mean values in Fig. 1, the difference between consecutive outputs was taken in each open-loop test,

$$\epsilon_k = Y_k - Y_{k-1}, \tag{9}$$

where the subscript k is the sampled drop instant, and ϵ_k is the fluctuation. The fluctuations shown in Fig. 7 exhibit a Gaussian-like distribution with a zero mean for drop volume and drop jetting velocity of different inks. A random walk can be used to model the process.

Since open-loop outputs were generated with a constant control input U, from the static relationship in Eq. (7), Eq. (9) can be rewritten as

$$\epsilon_k = U(\Theta_k - \Theta_{k-1}).$$

It suggests that the output fluctuation is equivalent to the fluctuation of model parameters. Therefore, it is reasonable to present the change of the model parameters in a random walk,

$$\Theta_{k+1} = \Theta_k + \mathbf{w}_{k+1}, \tag{10}$$

where $\mathbf{w}_k$ is the parameter uncertainty. Influence of process uncertainties, such as fluctuations in applied pressure and variations in printheads, is included in Eq. (10).

By considering the measurement noise $\mathbf{v}_k$, Eq (7) becomes

$$Y_k = F_k + G_k\bar{U}_k + \mathbf{v}_k = U_k\Theta_k + \mathbf{v}_k, \tag{11}$$

where $\mathbf{w}_k$ and $\mathbf{v}_k$ are assumed to have uncorrelated, zero-mean, Gaussian distributions with respective covariance matrices Q_k and R_k. Eqs. (10) and (11) are the stochastic plant model of drop volume and jetting velocity used for control design.

4. Control strategy

Because each drop is critical in on-demand functional printing for ensuring product functionality and geometry, the control objective is structured to regulate the volume and jetting velocity of each drop, that is, to minimize the one-step-ahead tracking error between the desired output Y_d and the system output Y_{k+1} with the known input–output information at the instant k. Given the use of Kalman algorithm in state estimation of random processes [30,31], using the similar fashion

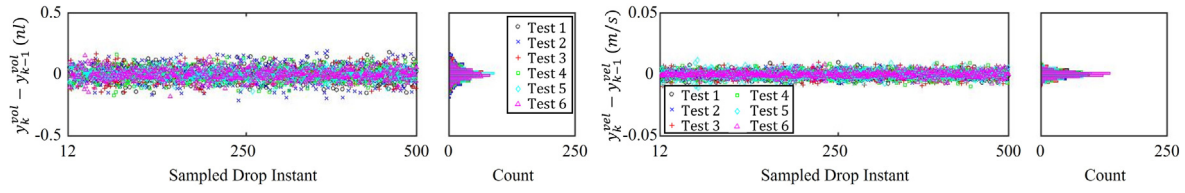

(a) DI Water: drop volume fluctuation.

(d) DI water: drop jetting velocity fluctuation.

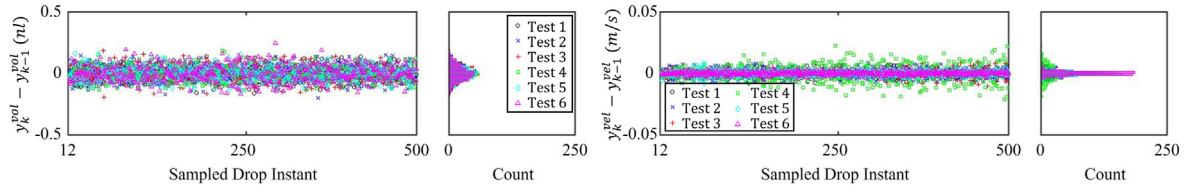

(b) Color ink: drop volume fluctuation.

(e) Color ink: drop jetting velocity fluctuation.

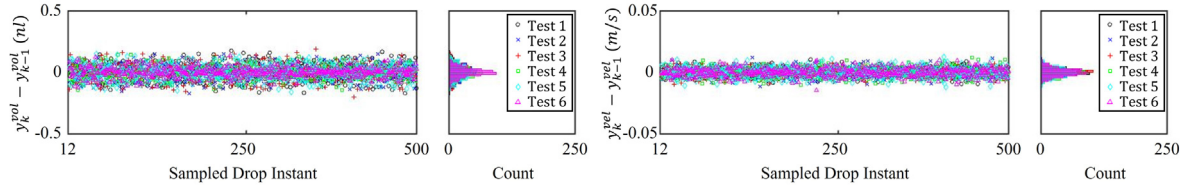

(c) GW mixture: drop volume fluctuation.

(f) GW mixture: drop jetting velocity fluctuation.

Fig. 7. Fluctuations in the outputs of DI water, color ink, and glycerol–water mixture, respectively, $\epsilon_k = Y_k - Y_{k-1}$.

of indirect adaptive control, the proposed control strategy comprises a Kalman estimator to estimate the one-step-ahead model parameter/state Θ_{k+1} and a controller which is a function of the estimated model parameters to reduce the tracking error at $k+1$.

Remark 1. In the following control strategy development, regression representation of the plant model $Y_k = U_k\Theta_k + \mathbf{v}_k$ shown in Eq. (11) is used for the estimation algorithm of model parameter vector Θ_k. The equivalent affine representation $Y_k = F_k + G_k\bar{U}_k + \mathbf{v}_k$ is employed for controller design. According to the equivalence of model representations shown in Eq. (7), the estimated model parameter vector $\hat{\Theta}_k$ can be arranged to the estimated model gain $\hat{G}_k$ and the estimated model bias $\hat{F}_k$.

4.1. Parameter estimation

Given the plant model Eqs. (10) and (11) and a control candidate U_{k+1}, the output Y at the sampling instant $k+1$ can be estimated by

$$\hat{Y}_{k+1} = U_{k+1}\hat{\Theta}_{k+1}. \tag{12}$$

$\hat{\Theta}_{k+1}$ is the estimated model parameter vector computed by the Kalman algorithm [32,33]

$$\hat{\Theta}_{k+1} = \hat{\Theta}_k + L_k(Y_k - \hat{Y}_k) = \hat{\Theta}_k + L_k(Y_k - U_k\hat{\Theta}_k), \tag{13}$$

where L_k is the Kalman gain, formulated as

$$L_k = P_kU_k^T(U_kP_kU_k^T + R_k)^{-1}. \tag{14}$$

In Eq. (14), P_k is the covariance matrix of parameter estimation error, $\tilde{\Theta}_k = \Theta_k - \hat{\Theta}_k$, given by

$$P_{k+1} = (I - L_kU_k)P_k + Q_{k+1}. \tag{15}$$

To prevent drifts in parameter estimation and ensure the boundedness of estimated parameters subject to system uncertainty, following the similar approach in [34,35], the parameter updating formula Eq. (13) is modified with a projection operator,

$$\hat{\Theta}_{k+1} = \hat{\Theta}_k + \mathbf{Pr}_{\hat{\Theta}_k}\big(L_k(Y_k - \hat{Y}_k)\big), \tag{16}$$

where

$$\mathbf{Pr}_{\hat{\theta}^i_k}(\bullet^i) = \begin{cases} 0 & \text{if } \hat{\theta}^i_k \geq \theta^i_{max} \text{ and } \bullet^i > 0, \\ 0 & \text{if } \hat{\theta}^i_k \leq \theta^i_{min} \text{ and } \bullet^i < 0, \\ \bullet^i & \text{otherwise.} \end{cases}$$

θ^i_k is the ith entry of the parameter vector Θ_k. The range of θ^i_k, $(\theta^i_{min}, \theta^i_{max})$, can be set to be larger than the confidence interval of the nominal model parameters in Eq. (8).

Given the measured output Y_k and the implemented control input U_k (equivalently $\bar{U}_k$), model parameter Θ_{k+1} can be estimated using Eqs. (14), (15) and (16). Drop volume and jetting velocity at the instant $k+1$ can be, in turn, estimated from Eq. (12) and used to solve the control input U_{k+1} (equivalently $\bar{U}_{k+1}$).

4.2. Control design

Based on the estimated system output $\hat{Y}_{k+1}$, the control candidate $\bar{U}_{k+1}$ is calculated by minimizing the expectation of a cost function of the squared one-step-ahead tracking error and the penalized control effort at the instant $k+1$ [36],

$$J = \min_{\bar{U}_{k+1}} E\left[(Y_d - \hat{Y}_{k+1})^T(Y_d - \hat{Y}_{k+1}) + \kappa\bar{U}^T_{k+1}\bar{U}_{k+1}\right], \tag{17}$$

where $Y_d = [y^{vol}_d \;\; y^{vel}_d]^T$, y^{vol}_d is the desired drop volume, y^{vel}_d is the desired drop jetting velocity, and κ is a positive weight coefficient.

The solution to Eq. (17) has the form of

$$\bar{U}_{k+1} = (\hat{G}^T_{k+1}\hat{G}_{k+1} + \kappa I)^{-1}\hat{G}^T_{k+1}(Y_d - \hat{F}_{k+1}), \tag{18}$$

where $\hat{G}_{k+1}$ and $\hat{F}_{k+1}$ are the estimated system gain and system bias which are regrouped from the estimated $\hat{\Theta}_{k+1}$ in Eq. (16).

Fig. 8 illustrates the proposed control strategy, where q^{-1} is the one-step delay operator. Eq. (18) is the control law used to control the plant model Eqs. (10) and (11) with the estimated parameters from Eqs. (14), (15) and (16).

Remark 2. The plant model Eq. (11) implies that the variations of control input and system output are proportionally correlated. When

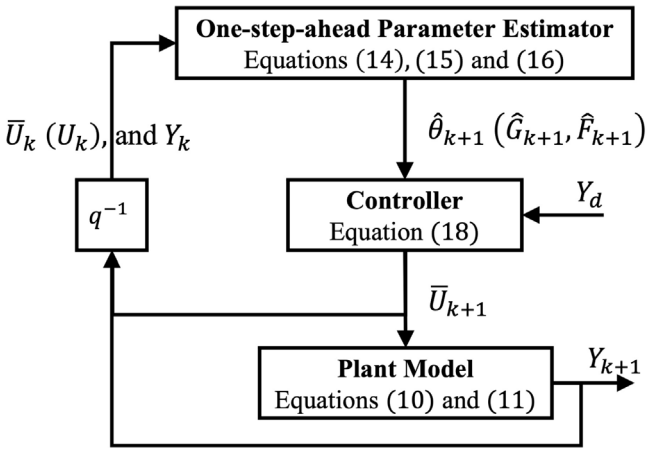

Fig. 8. Diagram of the proposed control strategy.

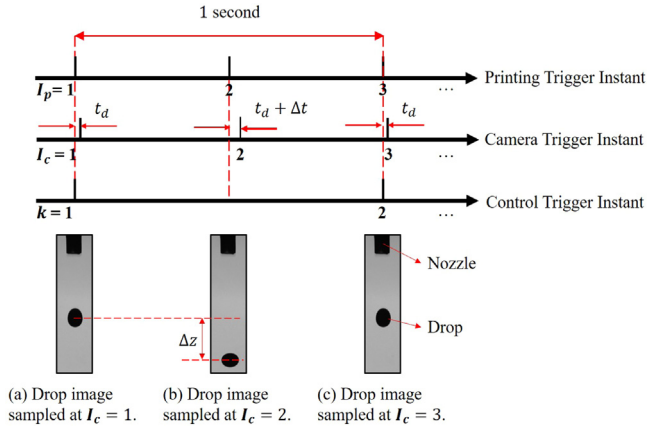

Fig. 9. Schematic of trigger timings for the printhead to jet a drop, for the camera to image the drop, and for the controller to update control parameters. (a) and (c) show drop images sampled at odd instants. (b) is a drop image sampled at an even instant.

system outputs are within acceptable thresholds, it may be advantageous to apply boundary layers (BL) around the control input to reduce unnecessary output fluctuation. Based on the impact of each control parameter on the output, the following BLs were proposed:

$$\begin{cases} u_{1,k} = u_{1,k-1} & \text{if } |y^{vel}_{k-1} - y^{vel}_d| \le T^{vel}, \\ u_{2,k} = u_{2,k-1} & \text{if } |y^{vol}_{k-1} - y^{vol}_d| \le T^{vol}. \end{cases} \tag{19}$$

T^{vel} and T^{vol} in Eq. (19) are the error threshold values for drop velocity and drop volume, respectively.

Remark 3. Following the similar approach in [37], boundedness of the expectation of spectral norms of the tracking error and the control input can be straightforwardly shown, respectively, with the projection operator used in the model parameter updating, which turns out to be bounded by the parameter estimation error. With certain similar assumptions given in [38–40], the boundedness and convergence of the parameter estimation error can be analyzed and are detailed in [23]. Then the closed-loop system is shown to be stable. For the situation that system outputs satisfy Eq. (19), it can be seen that the tracking error is bounded by the threshold while the control input is a constant.

5. Experimental validation of control algorithm

5.1. Control implementation

Three closed-loop experiments for each ink were conducted at different times using the proposed control strategy, see Fig. 8. The trigger timings used to implement the proposed control strategy are illustrated in Fig. 9. In-flight drops were imaged at drop jetting frequency of 2 Hz. Strobe trigger delay t_d with respect to the printhead trigger was adjusted until a distinct drop was clearly observed and stable in flight as seen in Fig. 9(a). Drop jetting velocity was calculated from two consecutive drops where an additional delay Δt was applied to even samples so that the drop jetting velocity can be approximated using Eq. (4). Drop volumes of the odd sampled drops were calculated using Eq. (2). The control inputs u_1 and u_2 were updated at the instant $k = 2, 3, \dots,$ in Fig. 9.

To implement the parameter estimation algorithm, covariances Q_k and R_k have to be specified. Because it is not feasible to image the same drop several times at the same distance away from the nozzle using one optical system, we assume that the measurement noise $\mathbf{v}_k$ is stationary. An open-loop experimental dataset was used to determine the measurement noise covariance R,

$$R = \begin{bmatrix} cov(y^{vol}, y^{vol}) & cov(y^{vol}, y^{vel}) \\ cov(y^{vel}, y^{vol}) & cov(y^{vel}, y^{vel}) \end{bmatrix} = \begin{bmatrix} 0.01 & 0.00007 \\ 0.00007 & 0.00002 \end{bmatrix},$$

where $cov(\cdot, \cdot)$ is the covariance of two random variables.

An innovation-based adaptive algorithm [41] was used to estimate the covariance Q_k of the parameter uncertainty $\mathbf{w}_k$,

$$\hat{Q}_k = L_k \Psi L_k^T, \tag{20}$$

where Ψ is defined as

$$\Psi = \frac{1}{N} \sum_{j=k-N+1}^{k} \psi_j \psi_j^T. \tag{21}$$

N is the moving window size, which was set to 5 in this work. The innovation sequence ψ_j is defined as the difference between the measured output and the estimated output,

$$\psi_j = Y_j - U_j \hat{\Theta}_j. \tag{22}$$

The nominal model parameters in Eq. (8) were used to initialize the Kalman estimation algorithm. Closed-loop experiments were implemented with

- **proposed controller w/o BL**: the controller described by Eq. (18) without the input boundary layer, which was described in [22, 23],
- **proposed controller w BL**: the controller Eq. (18) with the input boundary layer specified in Eq. (19).

The BL thresholds were determined from one standard deviation of fluctuation ϵ_k from Eq. (9), where $T^{vel} = 0.01$ m/s and $T^{vol} = 0.1$ nl. Maximum and minimum values of control inputs were included in practice, where

$$\begin{cases} \bar{U}_k = \bar{U}_{max} & \text{if } \bar{U}_k \ge \bar{U}_{max}, \\ \bar{U}_k = \bar{U}_{min} & \text{if } \bar{U}_k \le \bar{U}_{min}, \\ \bar{U}_k = \bar{U}_k & \text{otherwise.} \end{cases} \tag{23}$$

5.2. Experimental results

For each of the three ink types in Table 2, six open-loop experiments were conducted at different times using the same nozzle with the same control inputs u_1 and u_2. The control inputs were determined from the nominal model parameters in Eq. (8) to deliver the target volume

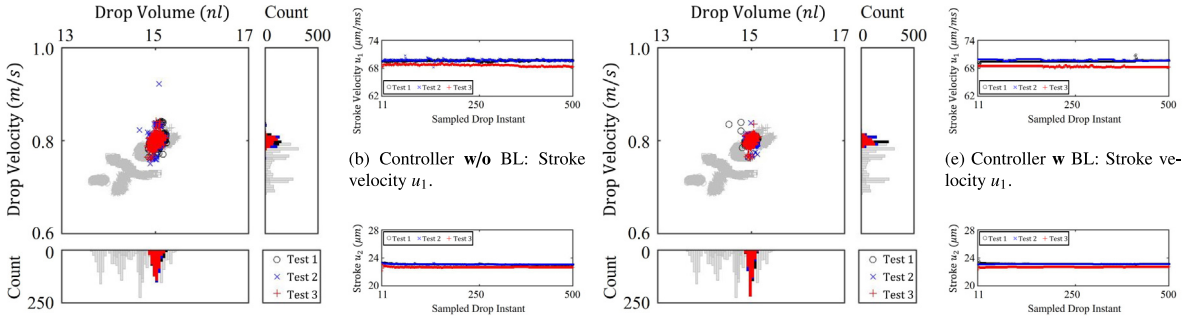

(a) Controller **w/o** BL: Outputs. (b) Controller **w/o** BL: Stroke velocity u_1. (c) Controller **w/o** BL: Stroke u_2. (d) Controller **w** BL: Outputs. (e) Controller **w** BL: Stroke velocity u_1. (f) Controller **w** BL: Stroke u_2.

Fig. 10. System inputs and outputs of DI water in different tests using the proposed controller w/o BL and w BL, respectively. Gray markers are the open-loop outputs. Color markers are the controlled outputs.

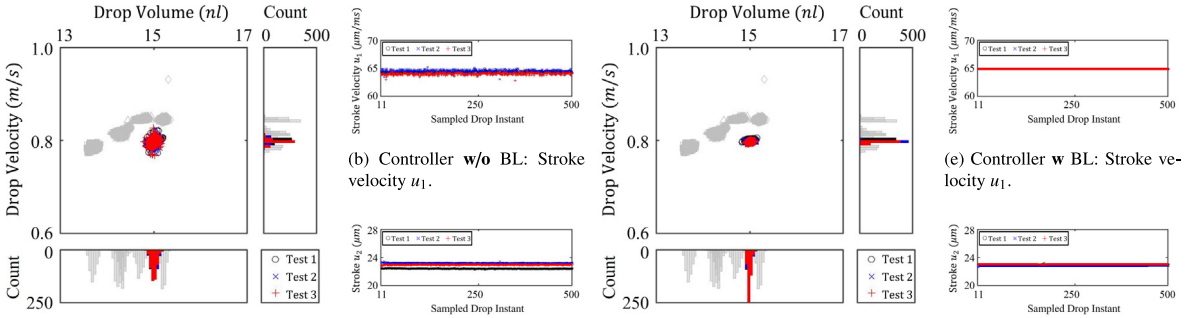

(a) Controller **w/o** BL: Outputs. (b) Controller **w/o** BL: Stroke velocity u_1. (c) Controller **w/o** BL: Stroke u_2. (d) Controller **w** BL: Outputs. (e) Controller **w** BL: Stroke velocity u_1. (f) Controller **w** BL: Stroke u_2.

Fig. 11. System inputs and outputs of color ink in different tests using the proposed controller w/o BL and w BL, respectively. Gray markers are the open-loop outputs. Color markers are the controlled outputs.

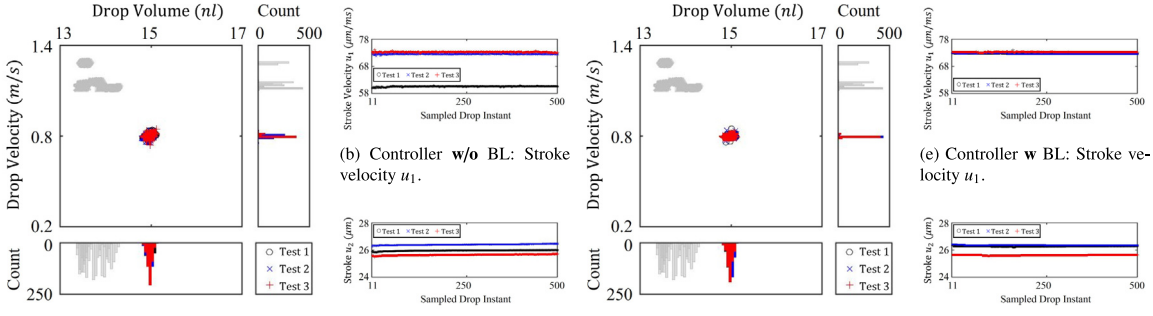

(a) Controller **w/o** BL: Outputs. (b) Controller **w/o** BL: Stroke velocity u_1. (c) Controller **w/o** BL: Stroke u_2. (d) Controller **w** BL: Outputs. (e) Controller **w** BL: Stroke velocity u_1. (f) Controller **w** BL: Stroke u_2.

Fig. 12. System inputs and outputs of GW mixture in different tests using the proposed controller w/o BL and w BL, respectively. Gray markers are the open-loop outputs. Color markers are the controlled outputs.

of 15 nl and target jetting velocity of 0.8 m/s. In each experiment, a total of 1000 drops were fired. 500 drop volumes and 500 drop jetting velocities were estimated for analysis.

In printing preparation, a printhead is routinely primed before printing to remove the "first drop" problem [42,43]. Therefore, in the following discussion, the first ten transient samples were removed.

Gray markers in Figs. 10–12 denote drop volume and jetting velocity from the six open-loop tests of DI water, color ink, and GW mixture. In general, the open-loop output deviates away from the target output, the center of the scatter plot. Although the implemented constant control input was calculated based on the nominal plant model to generate the desired characteristics, wide spreads of drop volume and drop jetting velocity present multi-modal distributions as seen in the associated histograms. These significantly limit DoD inkjet printing in dosage-sensitive and high-volume applications and suggest the need for closed-loop control.

In Figs. 10–12, color markers present the drop volume and drop jetting velocity of three tests controlled by the proposed controller w/o BL and w BL conducted at different times for DI water, color ink, and GW mixture, respectively. Unlike the open-loop results, for each ink, the outputs from the three tests controlled by the proposed controller w/o BL cluster around the center of the scatter plot with narrow spreads, which, in turn, present one distinguishable peak in the associated histogram. In Figs. 10–12(d), the results using the proposed controller w BL show much tighter spreads in both drop volume and drop jetting velocity without loss of tracking accuracy. The taller and thinner peaks in the associated histograms indicate that more drops have the desired characteristics. As summarized in Table 3, the tracking performance of the controlled drop volume and jetting velocity is remarkably improved, the mean values of which are close to the target. Large reductions in RSD demonstrate the effectiveness of the proposed

Table 3
Statistics of open-loop and controlled drop volumes (nl) and drop jetting velocities (m/s) of different inks. Target outputs are 15 nl and 0.8 m/s.

Ink	Statistics	Volume (nl)			Jetting velocity (m/s)		
		Open-loop	Controllerw/o BL[a]	Controllerw BL	Open-loop	Controllerw/o BL	Controllerw BL
DI Water	Mean	14.51	15.02	14.99	0.75	0.80	0.80
	RSD %[b]	3.11	0.49	0.36	4.53	1.38	0.88
Color Ink	Mean	14.41	15.00	14.98	0.82	0.80	0.80
	RSD %	3.23	0.42	0.26	2.56	0.75	0.25
GW Mixture	Mean	13.73	14.97	14.98	1.15	0.80	0.80
	RSD %	1.85	0.38	0.36	5.13	1.38	0.75

[a]Controller w/o BL is the controller described in [22,23].
[b]RSD (relative standard deviation) is calculated as the ratio of one standard deviation to the mean.

controller in regulating output variation. Around 80% variance reduction in drop volume and more than two thirds variance reduction in drop jetting velocity are observed for the inks under test in comparison to the open-loop results. The advantageousness of the boundary layer is also verified, see Table 3. Compared to the open-loop results, more than nine tens of variances of drop volume and jetting velocity are reduced in the result of color ink. Spreads of drop volume and jetting velocity of the other inks are also narrowed down to some extent with the added boundary layer to the proposed controller.

Drop volumes of the other 500 drops sampled at even instants, which were used for velocity calculation but for volume feedback, were estimated also. Their statistics are comparable to the results in Table 3.

Control inputs/parameters of the proposed controller w/o BL and w BL in three tests of DI water, color ink, and GW mixture are shown in Figs. 10–12(b)(c)(e)(f). It can be seen that fluctuations of control input and system output are correlated. The added boundary layers flatten the control inputs, resulting in less varying outputs.

6. Conclusion

This study proposes a control strategy to regulate drop volume and drop jetting velocity, with the use of a two-input two-output plant model developed from experimental printhead-ink calibration data. A one-step-ahead estimator for model parameters estimation is incorporated in the controller development. The efficacy of the proposed controller is experimentally verified with various inks by delivering drops with consistent volume and jetting velocity. Experiments also validate that including control boundary layers can further reduce output variance, i.e., less tracking-error-sensitive control may be preferred in regulating the stochastic process. This work benefits the modeling and control in commercial piezo-actuated drop-on-demand inkjet printers with different actuation mechanisms for printing different inks. Future work will concentrate on the integration of the proposed control strategy with learning-type controls in patterning different functional materials.

CRediT authorship contribution statement

Jie Wang: Conceptualization, Methodology, Software, Validation, Formal analysis, Investigation, Data curation, Visualization, Writing – original draft. **George T.-C. Chiu:** Conceptualization, Methodology, Visualization, Resources, Supervision, Writing – review & editing.

Declaration of competing interest

The authors declare that they have no known competing financial interests or personal relationships that could have appeared to influence the work reported in this paper.

Data availability

Data will be made available on request.

References

[1] Evans SE, Harrington T, Rodriguez Rivero MC, Rognin E, Tuladhar T, Daly R. 2D and 3D inkjet printing of biopharmaceuticals – A review of trends and future perspectives in research and manufacturing. Int J Pharm 2021;599:120443.
[2] Chou W-H, Gamboa A, Morales JO. Inkjet printing of small molecules, biologics, and nanoparticles. Int J Pharm 2021;600:120462.
[3] Hodul JN, Murray AK, Carneiro NF, Meseke JR, Morris J, He X, et al. Modifying the surface chemistry and nanostructure of carbon nanotubes facilitates the detection of aromatic hydrocarbon gases. ACS Appl Nano Mater 2020;3(10):10389–98.
[4] Bräuniger Y, Lochmann S, Grothe J, Hantusch M, Kaskel S. Piezoelectric inkjet printing of nanoporous carbons for micro-supercapacitor devices. ACS Appl Energy Mater 2021;4(2):1560–7.
[5] Zhu Z, Gong Z, Qu P, Li Z, Rasaki SA, Liu Z, et al. Additive manufacturing of thin electrolyte layers via inkjet printing of highly-stable ceramic inks. J Adv Ceram 2021;10(2):279–90.
[6] Hennig S, Shu Z, Gutzweiler L, Koltay P, von Stetten F, Zengerle R, et al. Paper-based open microfluidic platform for protein electrophoresis and immunoprobing. Electrophoresis 2022;43(4):621–31.
[7] Shield TW, Bogy DB, Talke FE. Drop formation by DOD ink-jet nozzles: A comparison of experiment and numerical simulation. IBM J Res Dev 1987;31(1):96–110.
[8] Xu Q, Basaran OA. Computational analysis of drop-on-demand drop formation. Phys Fluids 2007;19(10):102111.
[9] Morrison NF, Harlen OG. Viscoelasticity in inkjet printing. Rheol Acta 2010;49(6):619–32.
[10] Liu Y, Derby B. Experimental study of the parameters for stable drop-on-demand inkjet performance. Phys Fluids 2019;31(3):032004.
[11] Oktavianty O, Kyotani T, Haruyama S, Kaminishi K. New actuation waveform design of DoD inkjet printer for single and multi-drop ejection method. Addit Manuf 2019;25:522–31.
[12] Khalate AA, Bombois X, Babuška R, Wijshoff H, Waarsing R. Performance improvement of a drop-on-demand inkjet printhead using an optimization-based feedforward control method. Control Eng Pract 2011;19(8):771–81.
[13] Khalate AA, Bombois X, Scorletti G, Babuska R, Koekebakker S, de Zeeuw W. A waveform design method for a piezo inkjet printhead based on robust feedforward control. J Microelectromech Syst 2012;21(6):1365–74.
[14] Ezzeldin M, van den Bosch P, Weiland S. Experimental-based feedforward control for a DoD inkjet printhead. Control Eng Pract 2013;21(7):940–52.
[15] Tomaszewski G, Potencki J. Drops forming in inkjet printing of flexible electronic circuits. Circuit World 2017;43(1):13–8.
[16] Kiefer O, Fischer B, Breitkreutz J. Fundamental investigations into metoprolol tartrate deposition on orodispersible films by inkjet printing for individualised drug dosing. Pharmaceutics 2021;13(2):247.
[17] Haas R, Lohse S, Düllmann C, Eberhardt K, Mokry C, Runke J. Development and characterization of a drop-on-demand inkjet printing system for nuclear target fabrication. Nucl Instrum Methods Phys Res A 2017;874:43–9.
[18] Tröndle K, Rizzo L, Pichler R, Koch F, Itani A, Zengerle R, et al. Scalable fabrication of renal spheroids and nephron-like tubules by bioprinting and controlled self-assembly of epithelial cells. Biofabrication 2021;13(3):035019.
[19] Barton K, Mishra S, Alleyne A, Ferreira P, Rogers J. Control of high-resolution electrohydrodynamic jet printing. Control Eng Pract 2011;19(11):1266–73.
[20] Wang T, Kwok T-H, Zhou C, Vader S. In-situ droplet inspection and closed-loop control system using machine learning for liquid metal jet printing. J Manuf Syst 2018;47:83–92.
[21] Wang J, Chen X, Chiu G. Drop volume control in drop-on-demand inkjet printing. In: Proc. ASME dyn. syst. control conf.. 2019, V003T17A011.
[22] Wang J, Chiu GT-C. Control of drop volume and drop jetting velocity in inkjet printing. IFAC-PapersOnLine 2022;55(27):37–43.
[23] Wang J, Chiu GT-C. Drop-on-demand inkjet drop control with one-step look ahead estimation of model parameters. IEEE/ASME Trans Mechatronics 2023;28(4). [in press].

[24] Streule W, Lindemann T, Birkle G, Zengerle R, Koltay P. PipeJet: A simple disposable dispenser for the nano- and microliter range. J Assoc Lab Autom 2004;9(5):300–6.
[25] Wang J, Chiu GT-C. Data-driven drop formation modeling in nanoliter drop-on-demand inkjet printing. In: Proc. ASME dyn. syst. control conf.. 2020, V002T28A002.
[26] Landers RG, Barton K, Devasia S, Kurfess T, Pagilla P, Tomizuka M. A review of manufacturing process control. J Manuf Sci Eng 2020;142(11):110814.
[27] Snyder B, Yang M, Singhal S, Abed O, Sreenivasan S. Automated tuning of high-order waveforms for picoliter resolution jetting of rheologically challenging materials. Precis Eng 2019;56:143–55.
[28] Otsu N. A threshold selection method from gray-level histograms. IEEE Trans Syst Man Cybern 1979;9(1):62–6.
[29] Hirshfield L, Içten E, Giridhar A, Nagy ZK, Reklaitis GV. Real-time process management strategy for dropwise additive manufacturing of pharmaceutical products. J Pharm Innov 2015;10(2):140–55.
[30] Kiruluta A, Eizenman M, Pasupathy S. Predictive head movement tracking using a Kalman filter. IEEE Trans Syst Man Cybern B 1997;27(2):326–31.
[31] Zanni L, Boudec JYL, Cherkaoui R, Paolone M. A prediction-error covariance estimator for adaptive Kalman filtering in step-varying processes: Application to power-system state estimation. IEEE Trans Control Syst Technol 2017;25(5):1683–97.
[32] Palmer E, Pen W, Spanos CJ. Control of photoresist properties: A Kalman filter based approach. IEEE Trans Semicond Manuf 1996;9(2):208–14.
[33] Åström K, Wittenmark B. Problems of identification and control. J Math Anal Appl 1971;34(1):90–113.
[34] Fujimoto H, Bin Yao. Multirate adaptive robust control for discrete-time non-minimum phase systems and application to linear motors. IEEE/ASME Trans Mechatronics 2005;10(4):371–7.
[35] Ioannou PA, Sun J. Robust adaptive control. PTR Prentice-Hall Upper Saddle River, NJ; 1996.
[36] Goodwin GC, Sin KS. Adaptive filtering, prediction and control. Dover Publications; 2014.
[37] Goodwin GC, Ramadge PJ, Caines PE. Discrete time stochastic adaptive control. SIAM J Control Optim 1981;19(6):829–53.
[38] Jazwinski AH. Stochastic processes and filtering theory. New York: Academic Press; 1970.
[39] Guo L. Estimating time-varying parameters by the Kalman filter based algorithm: Stability and convergence. IEEE Trans Automat Control 1990;35(2):141–7.
[40] Reif K, Gunther S, Yaz E, Unbehauen R. Stochastic stability of the discrete-time extended Kalman filter. IEEE Trans Automat Control 1999;44(4):714–28.
[41] Mohamed AH, Schwarz KP. Adaptive Kalman filtering for INS/GPS. J Geod 1999;73(4):193–203.
[42] Taylor C, Lewis RH, Murcia A. Printer and method for priming an inkjet printhead. 2002, [U.S. Patent 6419343].
[43] Famili A, Palkar SA, Baldy WJ. First drop dissimilarity in drop-on-demand inkjet devices. Phys Fluids 2011;23(1):012109.

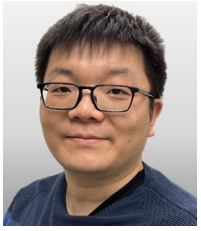

Jie Wang: received his M.S. degree in Mechanical Engineering from the Purdue University in 2016. He is currently working towards the Ph.D. degree with the School of Mechanical Engineering at Purdue University. His research interests include the modeling and control of dynamic systems and manufacturing processes, and mechatronics.

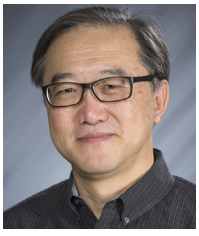

George T.-C. Chiu: is a Professor in the School of Mechanical Engineering with courtesy appointments in the School of Electrical and Computer Engineering and the Department of Psychological Sciences at Purdue University. Dr. Chiu received the B.S. degree in Mechanical Engineering from National Taiwan University in 1985 and the M.S. and Ph.D. degrees from the University of California at Berkeley, in 1990 and 1994, respectively. Before joining Purdue, he worked for the Hewlett-Packard Company, designing inkjet printer and multi-function devices. From 2011–14, he served as the Program Director for the Control Systems Program in the Engineering Directorate of the National Science Foundation. His current research interests are mechatronics and dynamic systems and control with applications to digital printing and imaging systems, digital fabrications, human motor control and robotics, motion and vibration perception and control. He is a Fellow of ASME and a Fellow of the Society for Imaging Science and Technology (IS&T) and a Senior Member of IEEE.